

## **Oxidation Kinetics of Hercynite Spinel for Solar Thermochemical Fuel Production**

**Authors:** Samantha L. Millican<sup>1</sup>, Iryna Androshchuk<sup>1</sup>, Justin T. Tran<sup>1</sup>, Ryan M. Trottier<sup>1</sup>, Alicia Bayon<sup>2</sup>, Yahya Al Salik<sup>3</sup>, Hicham Idriss<sup>3</sup>, Charles B. Musgrave<sup>1,4,5</sup>, and Alan W. Weimer<sup>1\*</sup>

### **Affiliations:**

<sup>1</sup>Department of Chemical and Biological Engineering, University of Colorado, Boulder, Colorado 80309, USA

<sup>2</sup>CSIRO Energy, PO Box 330, Newcastle, NSW 2300, Australia

<sup>3</sup>Center for Research and Development, Saudi Basic Industries Corporation (SABIC) at KAUST, Thuwal, Saudi Arabia

<sup>4</sup>National Renewable Energy Laboratory, Golden, CO 80401, USA

<sup>5</sup>Department of Chemistry, University of Colorado, Boulder, Colorado 80309, USA

\*Correspondence to: [alan.weimer@colorado.edu](mailto:alan.weimer@colorado.edu)

### **Abstract**

The development of an economically viable solar thermochemical fuel production process relies largely on identifying redox active materials with optimized thermodynamic and kinetic properties. Iron aluminate ( $\text{FeAl}_2\text{O}_4$ , hercynite) and cobalt-iron aluminate ( $\text{Co}_x\text{Fe}_{1-x}\text{Al}_2\text{O}_4$ ) have both been demonstrated as viable redox-active materials for this process. However, doping with cobalt produces a qualitative tradeoff between the thermodynamic and kinetic properties of hercynite by improving the reaction kinetics although, so far, at the expense of some drop in the overall activity per unit weight. In this work, we evaluate four spinel aluminate materials with varying cobalt contents ( $\text{FeAl}_2\text{O}_4$ ,  $\text{Co}_{0.05}\text{Fe}_{0.95}\text{Al}_2\text{O}_4$ ,  $\text{Co}_{0.25}\text{Fe}_{0.75}\text{Al}_2\text{O}_4$ , and  $\text{Co}_{0.40}\text{Fe}_{0.60}\text{Al}_2\text{O}_4$ ) to better understand the role of cobalt in the redox mediating properties of these materials and to quantify its effect on the thermodynamic and kinetic properties for  $\text{CO}_2$  reduction. A solid-state

kinetic analysis was performed on each sample to model its CO<sub>2</sub> reduction kinetics at temperatures ranging from 1200°C to 1350°C. An F1 model representative of first-order reaction kinetics was found to most accurately represent the experimental data for all materials evaluated. The computed rate constants, activation energies, and pre-exponential factors all increase with increasing cobalt content. High temperature in-situ XPS was utilized to characterize the spinel surfaces and indicated the presence of metallic states of the reduced cobalt-iron spinel, which are not present in un-doped hercynite. These species provide a new site for the CO<sub>2</sub> reduction reaction and enhance its rate through an increased pre-exponential factor.

### **Keywords**

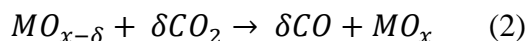
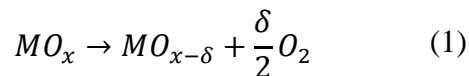
Solar thermal; thermochemical analysis; reaction kinetics, hercynite; CO<sub>2</sub> reduction; in situ XPS

## **1. Introduction**

Solar thermochemical fuel (STCF) production offers an attractive means to efficiently convert renewable solar energy into fuels such as H<sub>2</sub> and CO. By utilizing the entire solar spectrum and directly converting water or CO<sub>2</sub> into hydrogen or CO without generating electricity as an intermediate, STCF has the potential to achieve high conversion efficiencies [2]. In a two-step STCF process, solar radiation is directed to a central receiver containing a metal oxide redox active material. Heating this metal oxide to high temperatures in excess of 1000°C totally or partially reduces the metal oxide and generates oxygen gas [2-6]. In the second step, the reduced metal oxide is exposed to an oxidant, either steam or CO<sub>2</sub>, in order to oxidize the active material and produce either H<sub>2</sub> or CO fuels [7-9]. This step is exothermic and therefore is typically conducted at a lower temperature than the reduction step; however, isothermal STCF processes have been

demonstrated based on a pressure swing of the oxidant to modulate the oxygen chemical potential [10-15].

Metal oxides utilized for STCF production may either undergo stoichiometric reactions or oxygen vacancy reactions [9]. In the case of stoichiometric reactions, materials undergo either a crystallographic or a state-of-matter phase change during reduction and oxidation as is the case for the ferrite, zinc oxide, and tin dioxide cycles [5, 16-20]. While stoichiometric materials offer high extents of reduction and therefore high H<sub>2</sub> productivities, significant operational and materials challenges exist related to sintering, deactivation, and quenching of these active materials [18-24]. In the case of materials that undergo an oxygen vacancy mechanism, the reduction step results in the formation of oxygen vacancies within the crystal lattice of the material (partial reduction) rather than a crystallographic or state-of-matter transition [2, 6, 25]. STCF redox materials that operate via an oxygen vacancy mechanism have lower extents of reduction; however, they are preferred for this process because they have been demonstrated to be more stable over redox cycling than stoichiometric compounds and do not have the same operational challenges associated with quenching a gaseous active material present in volatile materials like ZnO [8, 26]. The reduction and oxidation reactions for an oxygen vacancy-mechanism material are summarized in Equations (1) and (2) for the case of CO<sub>2</sub> splitting where  $\delta$  is the extent of reduction of the metal oxide that depends on the identity of the active material, the reduction temperature, and the oxidant partial pressure.



In this work, the oxidation kinetics of spinel aluminate materials are investigated for CO<sub>2</sub> splitting. Solar thermochemical hydrogen production using this family of materials was first

demonstrated by Scheffe *et. al.* in 2010 who used atomic layer deposition (ALD) to deposit  $\text{CoFe}_2\text{O}_4$  on an alumina support [27]. They found that this process formed a cobalt-iron aluminate spinel upon redox cycling and produced substantially more  $\text{H}_2$  than unsupported  $\text{CoFe}_2\text{O}_4$  or  $\text{CoFe}_2\text{O}_4$  supported on zirconia, and was capable of operating at lower temperatures than the ceria cycle [27]. Although this cycle was originally hypothesized to operate via a stoichiometric reaction due to its close relation to the stoichiometric ferrite cycle, it has since been shown that this material undergoes an oxygen vacancy mechanism according to Equations (1) and (2) where the active metal oxide ( $\text{MO}_x$ ) is a mixed cobalt-iron aluminate spinel ( $\text{Co}_x\text{Fe}_{1-x}\text{Al}_2\text{O}_4$ ) [28].

Furthermore, it was demonstrated that hercynite produced substantially more  $\text{H}_2$  than the previously-demonstrated cobalt-iron aluminate spinel ( $259 \mu\text{mol H}_2/\text{g}$  in  $\text{FeAl}_2\text{O}_4$  vs.  $156 \mu\text{mol H}_2/\text{g}$   $\text{Co}_{0.4}\text{Fe}_{0.6}\text{Al}_2\text{O}_4$ ) [28]; however, an inherent tradeoff between the thermodynamic and kinetic properties between these materials was observed. While the  $\text{H}_2$  production in the cobalt-iron aluminate peaked and then dropped relatively quickly, the hercynite  $\text{H}_2$  production exhibited a lower peak and much longer tail. Hercynite was still producing  $\text{H}_2$  at the end of the cycle time while the cobalt-doped hercynite appeared to reach full conversion within the 15-minute oxidation cycle [28]. While this tradeoff between the thermodynamic and kinetic water splitting properties of the hercynite-family of materials has been observed and discussed, the kinetic differences have not been fully quantified nor has the role that cobalt plays in accelerating the kinetics been studied in detail. Further understanding the role of cobalt in the doped aluminate spinel will support the rational design of new compounds. Additionally, in the design of commercial-scale reactors for STCF production it is necessary to understand and model the intrinsic kinetic behavior of the relevant reactions [9].

The objective of this work is to develop a kinetic model of the oxidation step for CO<sub>2</sub> reduction by hercynite and cobalt-doped hercynite. Solid-state kinetic theory is utilized to quantify the activation energy and pre-exponential factor of CO<sub>2</sub> reduction by un-doped and Co-doped hercynite and to develop an understanding of the role of cobalt in the STCF production in these materials.

## 2. Methods

### 2.1 Experimental Methods

Materials were synthesized using a modified Pechini (citrate gel) method [29]. Metal nitrate salts Fe(NO<sub>3</sub>)<sub>3</sub>·9H<sub>2</sub>O, and Co(NO<sub>3</sub>)<sub>2</sub>·6H<sub>2</sub>O, and Al(NO<sub>3</sub>)<sub>3</sub>·9H<sub>2</sub>O (all > 98% purity) were dissolved in DI water. Citric acid was then added in a 1:4 ratio of citric acid to water. The solution was stirred and heated at 100°C for 30 minutes, then heated to 200°C and held without stirring until a viscous gel formed. The organics were vaporized away by heating the gel in a vacuum oven at 450°C for 12 hrs. The sample was then ground into a powder and an initial calcination was performed at 850°C for 8 hours in air to form the binary metal oxides. Final calcination was performed at 1350°C for 6 hours, then 1500°C for 6 hours in air. Attempts to measure the BET surface areas of these materials were not possible due to negligible pore volume giving an unmeasurable area within experimental errors. At this temperature all known metal oxides will sinter and experience a dramatic drop in their surface area. For example Al<sub>2</sub>O<sub>3</sub> calcined above 1200°C (the commonly known α-Al<sub>2</sub>O<sub>3</sub>) has typical BET surface areas between 2 and 0.1 m<sup>2</sup>/g. The formation of the spinel aluminate phase was confirmed using X-ray diffraction (XRD) and is shown in Figure S1 of the Supplemental Information (SI). Room temperature XRD patterns were obtained using a Bruker D8 Advance diffractometer with Cu Kα radiation. SEM images, which are shown for each composition in Figure S2-Figure S3, indicate that the powder samples had an

average particle size before and after cycling of  $67 \pm 34 \mu\text{m}$  and  $64 \pm 41 \mu\text{m}$ , respectively, as shown in Figure . The change in the particle size was not statistically significant ( $p = 0.32$ ). Considering that at this temperature pores contribution into the surface area is negligible then the extracted surface area from this size is  $0.02 \text{ m}^2/\text{g}_{\text{oxide}}$ .

Thermogravimetric analysis (TGA) (NETZSCH Jupiter F1) was used to track the extent of reaction during the  $\text{CO}_2$  reduction step.  $150 \text{ mg}$  ( $3.5 \times 10^{-3} \text{ m}^2$ )  $\pm 10 \text{ mg}$  ( $2 \times 10^{-3} \text{ m}^2$ ) of sample was loaded into an  $\text{Al}_2\text{O}_3$  TGA crucible. A plate crucible was utilized in order to minimize diffusion limitations from the gas stream to the sample and the sample size was varied to ensure that there were no mass transfer limitations due to the sample size. The temperature was ramped up to  $1450^\circ\text{C}$  at a rate of  $20^\circ\text{C}/\text{min}$  under an argon flow of  $70 \text{ mL}/\text{min}$  and held for 4 hours. The gas flow rate was increased until the rate of oxidation remained constant in order to avoid gas mass transfer limitations. Samples were reduced at  $1450^\circ\text{C}$  in inert Ar gas for 150 minutes and then the temperature was ramped down to the designated oxidation temperature ( $1350^\circ\text{C}$ ,  $1300^\circ\text{C}$ ,  $1250^\circ\text{C}$ , or  $1200^\circ\text{C}$ ) at a rate of  $20^\circ\text{C}/\text{min}$ . This temperature program is shown in Figure S5. Once the furnace reached the desired temperature, the flow was changed to  $70 \text{ mL}/\text{min}$  of  $50\% \text{ CO}_2/50\%$  argon and the sample mass was monitored. The gasses were mixed prior to entering the TGA chamber in order to eliminate the effect of gas mixing on the kinetic analysis. Once the mass reached steady state (between 2 and 8 hours depending on the sample and temperature), the sample was again reduced at  $1450^\circ\text{C}$  in inert gas for 150 minutes. Allowing the reaction to reach high conversions is essential for an accurate kinetic analysis.  $\text{CO}_2$  was chosen for this study in place of  $\text{H}_2\text{O}$  because  $\text{CO}_2$  and  $\text{H}_2\text{O}$  follow similar steady state behavior and have similar reduction enthalpies while  $\text{CO}_2$  circumvents experimental limitations in the temperatures accessible by the TGA equipment for steam experimentation [28, 30]. Samples of  $\text{FeAl}_2\text{O}_4$ ,  $\text{Co}_{0.05}\text{Fe}_{0.95}\text{Al}_2\text{O}_4$ ,

$\text{Co}_{0.25}\text{Fe}_{0.75}\text{Al}_2\text{O}_4$ , and  $\text{Co}_{0.4}\text{Fe}_{0.6}\text{Al}_2\text{O}_4$  were examined in this manner. Throughout this work, these samples are referred to based on the percentage of cobalt on the A-site of the spinel: 0% Co, 5% Co, 25% Co, and 40% Co, respectively. Because each sample was fully allowed to reach steady state, the conversion calculation for each sample and temperature was referenced to the steady state mass change measured for that sample and temperature. TGA mass data were converted to conversion ( $\alpha$ ) vs. time data via Equation (3).

$$\alpha = \frac{m_0 - m_t}{m_0 - m_\infty} \quad (3)$$

where  $m_0$  is the initial sample mass,  $m_t$  is the sample mass at time  $t$ , and  $m_\infty$  is the steady state mass at 100% conversion.

High temperature in-situ X-ray photoelectron spectroscopy (XPS) was utilized to characterize the surface composition of two samples ( $\text{FeAl}_2\text{O}_4$  and  $\text{Co}_{0.1}\text{Fe}_{0.9}\text{Al}_2\text{O}_4$ ). XPS was performed in a UHV system with a base pressure of  $2 \times 10^{-10}$  Torr equipped with SPECS XR50 dual anode Mg K $\alpha$  X-ray source and SCIENTA R3000 hemispherical electrostatic energy analyzer. The system is also equipped with a SPECS EBH-150 E-beam heater, which was utilized to heat the samples to the desired temperatures (1300°C for 5 min); this is the highest possible temperature that could be reached with this system while keeping the pressure low (in the  $10^{-9}$  torr range) avoiding contaminations or reoxidation by outgassed water molecules from the sample mount. The temperature of the samples was monitored with a Process Sensors Sirius pyrometer and a calibrated K-type thermocouple. ~~A lower temperature was utilized to account for the higher vacuum and approximately maintain a consistent oxygen chemical potential with the TGA experiments.~~ Approximately 20 mg of each material was pressed into 13 mm diameter pellets. The sample pellet was held on a tantalum sample holder by tantalum wires. The sample was then introduced to the prep chamber and pumped down until vacuum was recovered overnight. Once

the pressure in the prep chamber reached  $3 \times 10^{-9}$  Torr, the sample was introduced to the main analysis chamber. XPS data analysis was performed with a THERMO AVANTAGE software by Thermo Fisher Scientific. XPS spectra of Fe 2p, Co 2p, Al 2p, C 1s, and O 1s were collected. Typical acquisition conditions were as follows: Sample annealing time = 5 min; Pressure before annealing = low  $10^{-10}$  Torr; Pressure after annealing =  $3 \times 10^{-9}$  Torr; X-ray Power = 300W, V= 10 kV, I= 30 mA; Distance from the analyzer orifice = 4.5 cm; Angle to the analyzer with respect to the surface normal =  $0^\circ$ ; Pass energy = 50 eV; Scan rate = 0.1 eV/200ms. The analysis of Fe 2p XPS photoemission was straightforward while that of Co 2p proved more challenging because the Fe Auger lines contribute to the spectra in the Co region when using the Al  $K\alpha$  radiation source. Mg  $K\alpha$  stimulated emission was more conclusive, although the O KLL Auger emission interfered with the Co signal. This was deconvoluted for quantitative analysis. All spectra were calibrated with respect to adventitious carbon ( $sp^3$ ) at a binding energy of 285 eV.

## 2.2 Kinetic Theory

Solid-state kinetic modeling methods were implemented to determine a rate expression for each of the samples tested to analyze the effect of increasing cobalt content on the kinetic behavior of the oxidation reaction in spinel aluminates. The isothermal, isoconversional (model-free) method was first used to estimate the activation energy for each sample without modelistic assumptions [31, 32]. Using this method, the isothermal rate law in Equation (4) was utilized to determine the activation energy for the reaction at each conversion point.

$$g(\alpha) = Ae^{-E_a/RT}t \quad (4)$$

where  $A$  is the pre-exponential (frequency) factor,  $E_a$  is the activation energy,  $T$  is the temperature,  $R$  is the gas constant,  $t$  is the time, and  $g(\alpha)$  is the integral reaction model. Taking the natural

logarithm of Equation (4) results in Equation (5). A plot of  $\ln t$  versus  $1/T$  for each conversion gives the isoconversional activation energy.

$$\ln t_{\alpha} = -\ln\left(\frac{A}{g(\alpha)}\right) + \frac{E_{a,\alpha}}{RT} \quad (5)$$

Evaluation of the behavior of the isoconversional activation energy versus conversion allows for a determination of how many mechanisms control the rate-limiting step of the reaction. If the activation energy appears constant, then a single mechanism is responsible for the rate-limiting step [31]. A conventional isothermal model-fitting method was then applied to the range of constant isoconversional activation energies to determine the kinetic triplet:  $g(\alpha)$ ,  $A$ , and  $E_a$  [31, 33]. The rate constant,  $k$ , is determined for the model that best fits the data according to Equation (6) for each temperature studied. After determining the best fitting model and  $k$ ,  $E_a$  and  $A$  are obtained using the Arrhenius expression. The 17 solid-state kinetic models explored in this study are listed in Table 1.

$$g(\alpha) = kt \quad (6)$$

Table 1. Solid-state rate expressions for the 17 models evaluated in this study.

Model	Differential Form: $f(\alpha) = \frac{1}{k} \frac{d\alpha}{dt}$	Integral Form: $g(\alpha) = kt$
<i>Nucleation Models</i>		
Power law (P2)	$2\alpha^{\frac{1}{2}}$	$\alpha^{\frac{1}{2}}$
Power law (P3)	$3\alpha^{\frac{2}{3}}$	$\alpha^{\frac{1}{3}}$
Power law (P4)	$4\alpha^{\frac{3}{4}}$	$\alpha^{\frac{1}{4}}$
Avrami-Erofe'ev (A2)	$2(1-\alpha)[- \ln(1-\alpha)]^{\frac{1}{2}}$	$[- \ln(1-\alpha)]^{\frac{1}{2}}$
Avrami-Erofe'ev (A3)	$3(1-\alpha)[- \ln(1-\alpha)]^{\frac{2}{3}}$	$[- \ln(1-\alpha)]^{\frac{1}{3}}$

Avarami-Erofe'ev (A4)	$4(1 - \alpha)[- \ln(1 - \alpha)]^{\frac{3}{4}}$	$[- \ln(1 - \alpha)]^{\frac{1}{4}}$
Prout-Tompkins (B1)	$\alpha(1 - \alpha)$	$\ln\left(\frac{\alpha}{1 - \alpha}\right)$
<i>Geometrical Contraction Models</i>		
Contracting area (R2)	$2(1 - \alpha)^{\frac{1}{2}}$	$1 - (1 - \alpha)^{\frac{1}{2}}$
Contracting volume (R3)	$3(1 - \alpha)^{\frac{2}{3}}$	$1 - (1 - \alpha)^{\frac{1}{3}}$
<i>Diffusion Models</i>		
1D diffusion (D1)	$\frac{1}{2}\alpha$	$\alpha^2$
2D diffusion (D2)	$[- \ln(1 - \alpha)]^{-1}$	$(1 - \alpha) \ln(1 - \alpha) + \alpha$
3D diffusion (D3)	$\frac{3}{2}(1 - \alpha)^{\frac{2}{3}} \left[1 - (1 - \alpha)^{\frac{1}{3}}\right]^{-1}$	$\left[1 - (1 - \alpha)^{\frac{1}{3}}\right]^2$
Ginstling-Brounshtein (D4)	$\frac{3}{2} \left( (1 - \alpha)^{-\frac{1}{3}} - 1 \right)$	$1 - \frac{2}{3}\alpha - (1 - \alpha)^{\frac{2}{3}}$
<i>Reaction-Order Models</i>		
Zero-order (F0)	1	$\alpha$
First-order (F1)	$1 - \alpha$	$- \ln(1 - \alpha)$
Second-order (F2)	$(1 - \alpha)^2$	$(1 - \alpha)^{-1} - 1$
Third-order (F3)	$(1 - \alpha)^3$	$\frac{1}{2}((1 - \alpha)^{-2} - 1)$

### 3. Results and Discussion

In order to understand the role of cobalt in the redox behavior of the spinel aluminates, four materials with different cobalt compositions were evaluated: 0% Co, 5% Co, 25% Co, and 40% Co. Here, we report and discuss the general findings from the TGA results and the kinetic triplet

for each system studied using solid-state kinetic modeling. Results from XPS of 0% and 10% Co samples, both as prepared and reduced at 1300°C, are presented to further support the results from the kinetic analysis.

### 3.1 Thermogravimetric Results

The conversion versus time data extracted from the TGA experiments for each of the samples analyzed are shown in in Figure 1 for CO<sub>2</sub> reduction at 1350°C and clearly illustrate the effect of increasing the cobalt concentration on increasing reaction rates. Additional data for each material at four CO<sub>2</sub> splitting temperatures ranging from 1200 to 1350°C with a constant metal-oxide reduction temperature of 1450°C are shown in Figure S6.

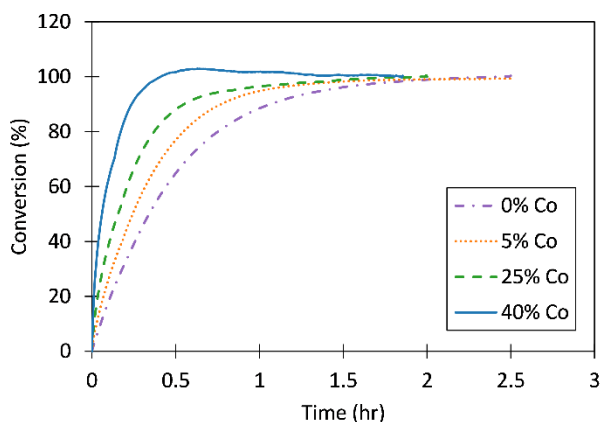


Figure 1. A comparison of the extracted conversion versus time data for each of the samples tested at 1350°C.

In addition to conversion, CO production at each temperature was extracted under the assumption that all mass gain of the sample resulted from incorporation of oxygen from CO<sub>2</sub> during the formation of CO in accordance with Equation (2). The resulting CO production is shown in Figure 2. Measured

CO productions reach up to 997  $\mu\text{mol CO/g}$  for the un-doped hercynite sample at 1200°C. The addition of cobalt in the hercynite material results in a substantial decrease in CO production, with up to an 80% decrease at 1200°C between the 0% Co and 40% Co samples. In previous studies of water splitting with  $\text{Co}_{0.4}\text{Fe}_{0.6}\text{Al}_2\text{O}_4$  in a stagnation flow reactor (SFR), 156  $\mu\text{mol H}_2/\text{g}$  was produced at an oxidation temperature of 1350°C [28]. This is in good agreement with the CO

production achieved by the TGA in this experiment (158  $\mu\text{mol CO/g}$  at 1350°C by the 40% Co sample). This is expected because the required reduction enthalpies for splitting water and carbon dioxide are similar and the redox reaction is expected to behave similarly [28, 34]. This agreement also validates the assumption that the mass gain can be attributed to the production of CO gas via Equation (2). The fuel productions from the 0% Co sample in this study and that measured in

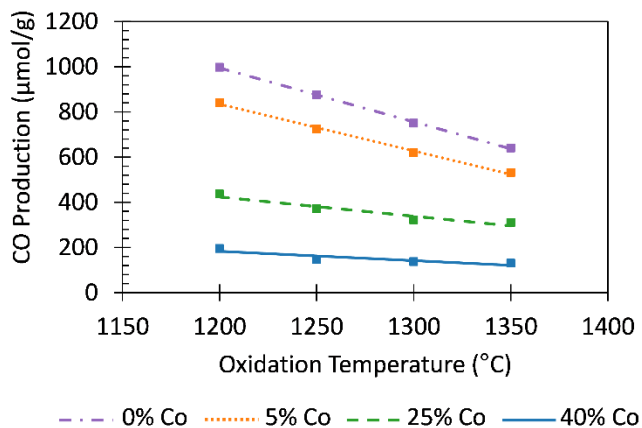


Figure 2. CO productivities for all four samples at each temperature studied under the assumption that all mass change in the sample is associated with CO.

state conversion, while the 40% Co sample reached greater than 90% of its steady state conversion after 15 minutes.

previous SFR experimental studies cannot be compared because the sample tested in the SFR was only oxidized for 15 minutes and was not allowed to reach steady state [28]. The curves plotted in Figure 1 suggest that only a fraction of the mass gain occurs within the first 15 minutes for the 0% Co sample, reaching approximately 40% of its steady

### 3.2 Isoconversional Kinetic Modeling

For each of the compounds studied, the isoconversional (model-free) method was used to determine the range of conversions over which  $E_a$  is stable and thus the system is controlled by a

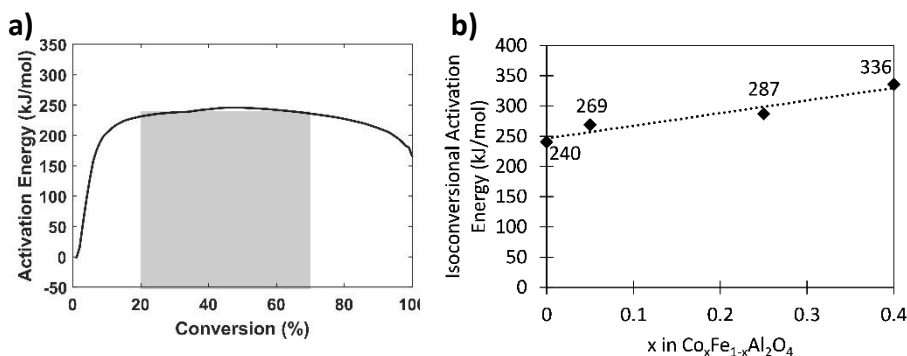


Figure 3. a)  $E_a$  over the conversion range determined using an isoconversional method for 0% Co.  $E_a$  is stable over the range  $\alpha = 0.20 - 0.70$ . b)  $E_a$  for each compound studied determined using the isoconversional (model-free) method.

single mechanism. All materials exhibited similar behavior with constant  $E_a$  over the range  $\alpha = 0.20 - 0.70$

of conversions was utilized for the model-fitting method of analysis described in the next section.

The activation energies estimated using the isoconversional method for each compound are plotted in Figure 3b.  $E_a$  increased with higher cobalt content from 240 kJ/mol for the 0% Co sample to 336 kJ/mol for the 40% sample. These values serve as a comparison point for  $E_a$  determined in combination with  $g(\alpha)$  and  $A$  using the model-fitting method.

### 3.3 Conventional Model Fitting Approach

Utilizing the range of conversions determined with the isoconversional method, a conventional isothermal model-fitting method was then used to determine  $g(\alpha)$ ,  $A$ , and  $E_a$ . A linear fit of the 17 solid-state kinetic models tabulated in Table 1 was performed to determine  $k$  of the model that best fits the data according to Equation (6). These models include nucleation models, geometrical contraction models, diffusion models, and reaction order models. The goodness of fit of each of these models for the case of 0% Co is shown in Figure S7. A first-order reaction model (F1) has the best fit to the experimental data for all systems evaluated with a

coefficient of determination  $> 0.98$  in all cases over the range  $\alpha = 0.20 - 0.70$ . This is in line with the study of other materials for solar thermochemical fuel production which show a similar F-family rate-limiting step [34-36], although combined reaction order and diffusion models have been identified for some materials [35, 37]

The resulting rate constants for each material from the F1 model are shown in Figure 4a. The  $E_a$  and  $A$  computed for each material from  $k$  using the Arrhenius equation are displayed in Figure 4b while the resulting conversion versus time curves are plotted in Figure S8. As the qualitative results in Figure 1 indicate, increasing the cobalt content in the spinel aluminates increases the rate constant. The activation energies determined from this model-fitting approach show excellent agreement with those determined from the isoconversional model-free method with less than a 5% difference for all compounds. While the overall rate constant increases with increasing cobalt content, this increase in rate is driven by an increase in the pre-exponential factor because a partially offsetting increase in the activation energy also results from increasing cobalt content. It has previously been hypothesized that the presence of cobalt further accelerated the overall water splitting surface reaction [28]. Based on the results presented here, cobalt increases the reaction rate not by lowering  $E_a$  of the overall reaction, but by increasing  $A$  by some other effect, such as increasing the number of active sites, in this case, oxygen vacancies.

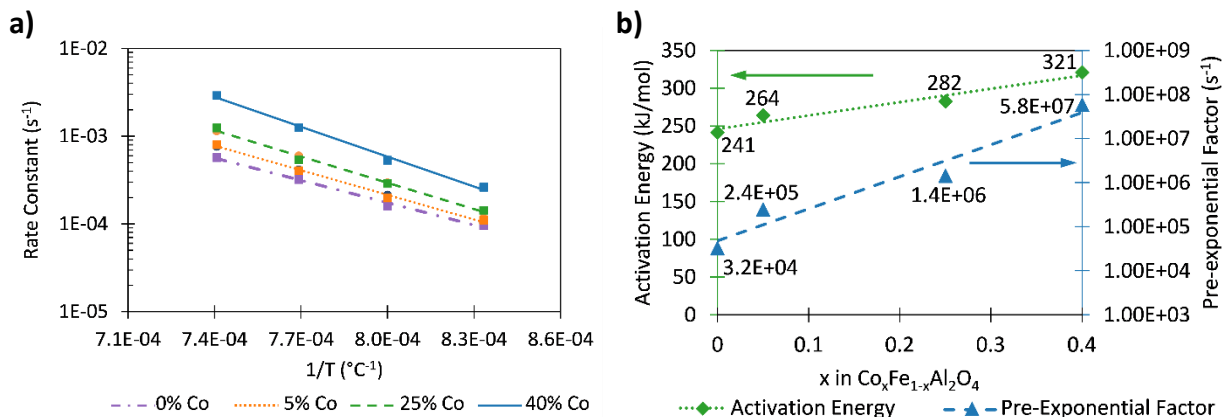


Figure 4. a) Rate constant ( $k$ ) for each of the materials studied at four oxidation temperatures. The rate constant increases with increasing temperature and increasing Co concentration. b) Activation energy (green) and pre-exponential factor (blue) determined from a conventional isothermal model-fitting method using the Arrhenius equation.

The results illustrated in Figure 2 and Figure 4 highlight the tradeoff between the thermodynamic and kinetic performance caused by the incorporation of cobalt into the hercynite spinel structure. While  $k$  increased by more than a factor of 4 for the 40% Co sample relative to the 0% Co sample at an oxidation temperature of  $1350^{\circ}C$ , for these same samples and oxidation conditions, the CO production decreased by 75% with the incorporation of 40% Co. This effect suggests that Co concentration offers a clear tuning parameter in the design of larger scale systems as it could be precisely tuned for optimal kinetic and thermodynamic performance of a given reactor configuration.

The F1 rate expression identified here represents an overall mechanism whose kinetics are controlled by an Arrhenius reaction with a first-order rate-limiting step. In the  $CO_2$  reduction reaction by the spinel aluminates studied here, an F1 reaction may be limited by  $CO_2$  adsorption,  $CO_2$  dissociation/surface vacancy elimination, or CO desorption. The identification of the F1 mechanism does not enable the determination of which of these processes is rate-limiting; however, based on several evaluations of typical values of  $A$  and their rate-limiting steps for a wide variety of reactions on different surfaces, the values  $A$  of  $10^4 - 10^8 s^{-1}$  reported in Figure 4 are

higher than typical first-order values of  $A$  for adsorption ( $10^{-1} - 10^4 \text{ s}^{-1}$ ) and lower than those for desorption ( $10^{12} - 10^{18} \text{ s}^{-1}$ ) [38-43].

Therefore, the  $E_a$  and  $A$  determined in this work for a surface mediated F1 reaction mechanism indicate that the reaction is limited by  $\text{CO}_2$  dissociation/surface vacancy elimination so the availability, local environment, and energy of oxygen vacancies at the surface will play a key role in the kinetic behavior of the material. The lower CO production measured in the samples with higher cobalt content may be linked to the total number of oxygen vacancies formed during the thermal reduction process or it could be related to further reaction of CO with metallic Co (if present) to form  $\text{Co}_2\text{C}$  as identified in Fischer Tropsch reactions [44, 45]. This is known as Boudouard reaction (Experimental and Kinetic Analysis for particle scale 2 modeling of a CuO-Fe<sub>2</sub>O<sub>3</sub>-Al<sub>2</sub>O<sub>3</sub> oxygen carrier during 3 reduction with CO in Chemical Looping combustion applications, Jarrett Riley, Ranjani Siriwardane, Hanjing Tian, William Benincosa, and James Poston (Applied Energy 228:1515-1530 (2018)). where two molecules of CO react with a metal center giving one molecule of  $\text{CO}_2$  and depositing carbon. Carbon deposited can be amorphous or may form a metal carbide. If this reaction occurs then a complete cycle of  $\text{CO}_2$  reduction to CO ( $2 \text{ CO}_2 + 2 \text{ V}_\text{O} \rightarrow 2 \text{ CO} + 2 \text{ O}_\text{s}$ ) and the latter further reacting to  $\text{CO}_2$  ( $2 \text{ CO} \rightarrow \text{C}_\text{s} + \text{CO}_2$ ) results in one carbon atom and two oxygen atoms, consuming two  $\text{V}_\text{O}$  ( $\text{CO}_2 + \text{V}_\text{O} \rightarrow 2 \text{ O}_\text{s} + \text{C}$ ); where  $\text{s}$ , and  $\text{V}_\text{O}$  stand for surface and oxygen vacancy, respectively. XRD analysis did not indicate the presence of  $\text{Co}_2\text{C}$  species after  $\text{CO}_2$  reduction possibly because if any its formation will be too small to detect. Yet the fact that the materials maintained many cycles indicate that if the above set of reactions occurs it is not dominant. The higher pre-exponential factor in Co-containing samples when compared to that of the samples without Co indicates that the Co may increase the rate by either offering an alternative reaction pathway or by increasing the concentration of reactive

sites (oxygen vacancies) near the surface. As in-situ XPS analysis shows below, the overall concentration of surface and near-surface reduced states is higher when Co is introduced into hercynite suggesting that the number of oxygen vacancies (or centers to abstract oxygen anions from CO<sub>2</sub>) has increased.

### 3.4 XPS Analysis

The positive correlation observed between  $A$  and  $E_a$  has been noted in many catalytic and/or surface mediated processes [39, 40, 46-50]. However, to further probe the surface and near surface electronic states of the spinel aluminates and discover the origin of the increased reaction rate in the cobalt-containing samples, in-situ XPS was conducted on two samples (0% and 10% Co). Each were analyzed as-prepared at 25°C and in-situ upon heating in ultra-high vacuum ( $< 10^{-9}$  Torr) at 1300°C. The C 1s, O 1s, and Al 2p core emission lines are shown and described in Figure S9 of the SI. The main changes between the room temperature and reduced samples relevant to the CO<sub>2</sub> splitting reaction are indicated by the XPS Fe 2p and Co 2p emission lines. In the Fe 2p region of the spectra of the 25°C sample (Figure 5a), both Fe<sup>2+</sup> and Fe<sup>3+</sup> cations are observed. The presence of Fe<sup>3+</sup> cations in FeAl<sub>2</sub>O<sub>4</sub> has been reported previously and may result from the formation of small clusters of Fe<sub>2</sub>O<sub>3</sub> /Fe<sub>3</sub>O<sub>4</sub> on the surface, although Mössbauer spectroscopy indicates that some octahedrally coordinated Fe cations are in the +3 oxidation state in pure FeAl<sub>2</sub>O<sub>4</sub> [51]. Satellite signals for both oxidation states are found at ca. 6 eV above the main core lines, although the Fe<sup>2+</sup> satellite is more pronounced than that of Fe<sup>3+</sup> [52].

Figure 5b displays the same Fe 2p XPS emission lines for FeAl<sub>2</sub>O<sub>4</sub> after it was heated to 1300°C under vacuum with the main difference being the ratio of Fe<sup>2+</sup> to Fe<sup>3+</sup>. The ratio before heating is measured to be 1.89:1 while heating increased this ratio to 2.84:1 (Table 2) which

provides evidence of reduction of Fe cations upon heating. There is also a small presence of  $\text{Fe}^0$  (0.36 %). In total, the reduction decreased the population of  $\text{Fe}^{3+}$  by about 25%.

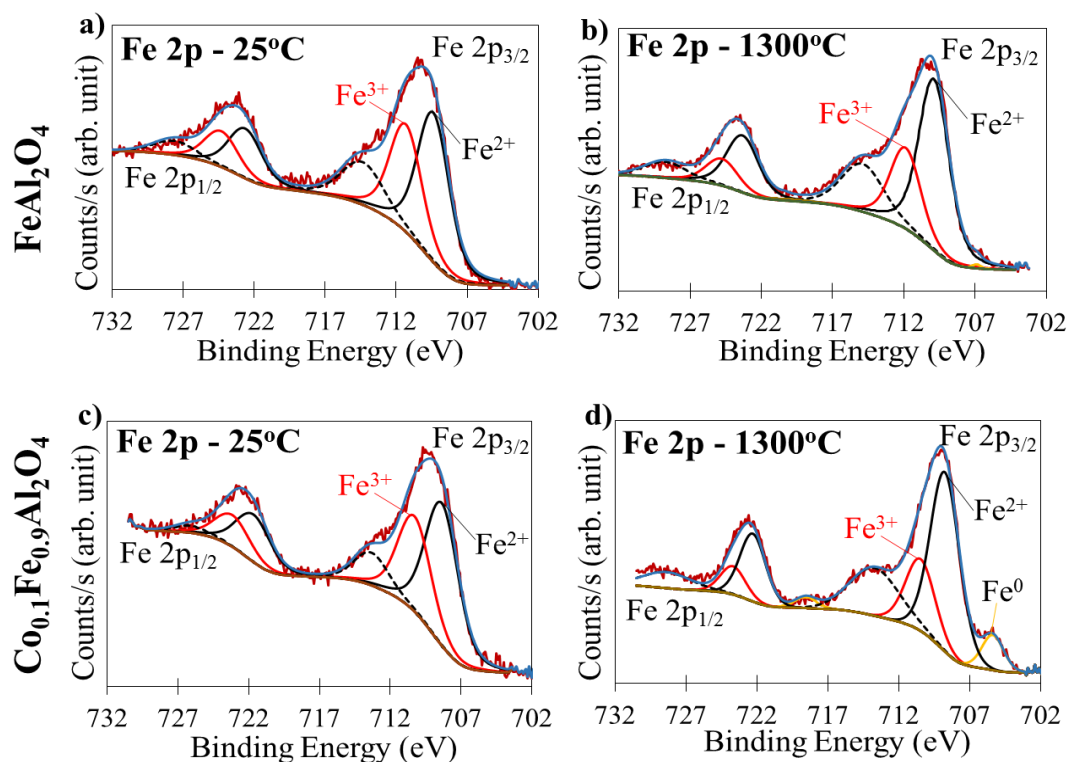


Figure 5. XPS Fe 2p spectra of (a,b) 0% Co and (c,d) 10% Co before and after heating in ultra-high vacuum at 1300°C. Heating causes a considerable increase of the Fe  $2p_{3/2,1/2}$  lines attributed to  $\text{Fe}^{2+}$  in both samples and the appearance of peaks related to  $\text{Fe}^0$  in the  $\text{Co}_{0.1}\text{Fe}_{0.9}\text{Al}_2\text{O}_4$  sample.

A similar analysis was conducted for the Co containing spinel material. As Figures 5c-d show, the  $\text{Fe}^{2+}$  contribution increased and a non-negligible amount of  $\text{Fe}^0$  appeared upon heating. The ratio of  $\text{Fe}^{x+}/\text{Fe}^{3+}$  increased from 1.81:1 to 3.92:1 indicating a decrease in the  $\text{Fe}^{3+}$  population by ~43%, as shown in Table 2. This provides evidence that the presence of Co cations resulted in further reduction of  $\text{Fe}^{3+}$  to  $\text{Fe}^{2+}$  and of  $\text{Fe}^{2+}$  cations to  $\text{Fe}^0$  which is not observed in the absence of Co. Similar consecutive cation reduction reactions have previously been observed by in-situ XPS for other systems [53]. This results in increasing the number of sites that can abstract oxygen anions from  $\text{CO}_2$  to produce CO.

The Co 2p region of the XPS spectra is more complex to analyze and we have opted to provide only qualitative information (Figure 6). Using an Al  $K\alpha$  source for photoexcitation produced spectra with Fe Auger lines in the Co region. Therefore, we opted to use a Mg  $K\alpha$  X-Ray source which resulted in some contribution from the O KLL Auger signal in the Co 2p region, but the remaining region was adequate for the type of analysis conducted. The doublet at 795 and 801.5 eV in Figure 6a can be attributed to Co 2p<sub>1/2</sub> of Co<sup>2+</sup>/Co<sup>3+</sup> and its satellite. It is worth noting that the binding energy shift between Co<sup>3+</sup> and Co<sup>2+</sup> is about 0.3 eV, which is within the detection limit of the XPS used [54]. From the Co 2p<sub>1/2</sub> and spin orbit splitting value of 15 eV, we fit the Co 2p<sub>3/2</sub> for both the main peak and its satellite [55]. The large peak at 786 eV and the small peak at 777 eV are due to the O KLL Auger signal with the latter overlapping the XPS Co 2p<sub>3/2</sub> of Co<sup>0</sup> emission. As Figure 6b shows, heating the oxide to 1300°C resulted in an increase of the peak at 777 eV that we attribute to Co<sup>0</sup>.

Overall, heating Co<sub>0.1</sub>Fe<sub>0.9</sub>Al<sub>2</sub>O<sub>4</sub> in vacuum at 1300°C resulted in the reduction of a fraction of the Fe and Co cations into their metallic states. This may be due to the presence of small

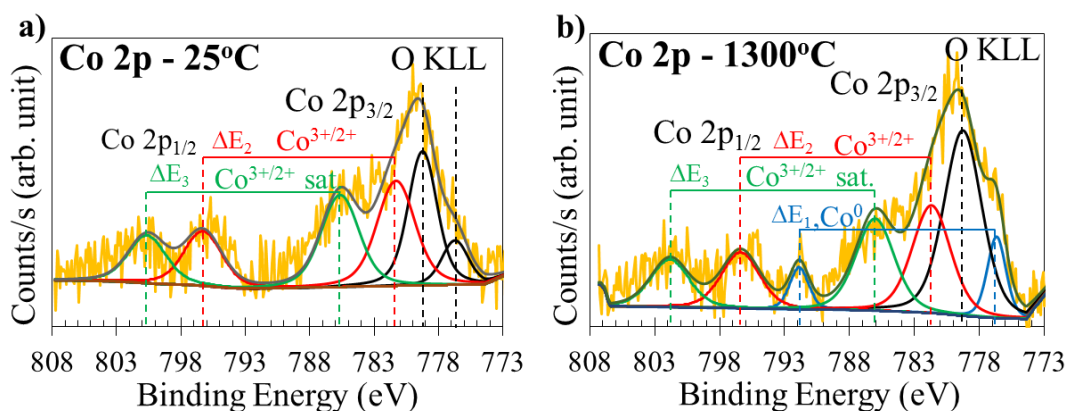


Figure 6. XPS core lines of Co 2p in the 10% Co sample (a) before and (b) after heating in ultra-high vacuum at 1300°C. The Co<sup>3+/2+</sup> peak at about 780 eV (with a large contribution from the Auger line, O KLL) increases after heating which might be due to increasing amounts of reduced Co cations when compared to the as prepared sample. This, together with the increased intensity of the 777 eV line mostly attributed to Co<sup>0</sup>, indicate the reduction of Co cations.  $\Delta E_1$ ,  $\Delta E_2$  and  $\Delta E_3$  are the spin orbit splitting of Co<sup>0</sup>, Co<sup>x+</sup> and a satellite.

transition metal oxide clusters, in the form of Fe-O-Co, Fe-O-Fe, and/or Co-O-Co sites on the surface, which give rise to these metallic species upon heating. It is also possible that electrons diffuse between phases across their interface. Our XPS data indicate that in 0% Co  $\text{Fe}^{3+}$  reduces to  $\text{Fe}^{2+}$  while in 10% Co  $\text{Fe}^{3+/2+}$  and  $\text{Co}^{3+/2+}$  reduce to  $\text{Fe}^0$  and  $\text{Co}^0$ . During surface and near surface oxidation by the  $\text{CO}_2$  splitting reaction two electrons associated with a metallic species are transferred to an oxygen atom which is reincorporated into the lattice in the place of an oxygen vacancy. While this reaction requires two  $\text{Fe}^{2+}$  cations in  $\text{FeAl}_2\text{O}_4$  to be oxidized to  $\text{Fe}^{3+}$ , in the presence of metallic  $\text{Fe}^0$  or  $\text{Co}^0$ , only one neighboring transition metal site is required. While ideally one can monitor this with XPS O1s, O1s signal of power oxide materials is difficult to study because of any traces of water in the environment (even at  $10^{-10}$  torr) may change its surface concentration invalidating the quantitative analysis. That is because the sticking coefficient of water on reduced metal oxides is near unity. By monitoring the Fe2p and Co2p lines we found that heating the hercynite containing Co cations resulted in increasing the amounts of metallic Fe when compared to  $\text{FeAl}_2\text{O}_4$  alone. This occurred in addition to the reduction of Co cations to metallic Co. The reduction to metallic state would inevitably lead to structural collapse or distortion, yet this seems to be reversible, because the  $\text{CO}_2$  reduction cycles experiments. Therefore it is not possible to discern phase segregation from cationic reduction in a distorted structure. There might also be a blocking effect of the bulk-spinel with increasing Co content and that can explain the fast  $\text{CO}_2$  reduction and at the same time the weaker overall conversion. We propose that the reduction of  $\text{Fe}^{3+/2+}$  and  $\text{Co}^{3+/2+}$  to metallic species, which occurs in the cobalt-containing sample, provides these new sites for the  $\text{CO}_2$  splitting reaction which in turn is postulated to enhance the reaction rate through an increased pre-exponential factor.

Table 2. Extracted percentage of Fe oxidation states from XPS Fe 2p lines in  $\text{FeAl}_2\text{O}_4$  and  $\text{Co}_{0.10}\text{Fe}_{0.90}\text{Al}_2\text{O}_4$  before and after heating in vacuum at  $1300^\circ\text{C}$ . All lines are corrected to the relative sensitivity of the elements.

Compound	Temperature	$\text{Fe}^0$ %	$\text{Fe}^{2+}$ %	$\text{Fe}^{3+}$ %	$\text{Fe}^x/\text{Fe}^{3+}$	$\text{Fe}^x/\text{Fe}^{3+}$ adjusted <sup>1</sup>
$\text{FeAl}_2\text{O}_4$	$25^\circ\text{C}$	0	65.5	34.5	1.89	-
	$1300^\circ\text{C}$	0.36	73.7	25.9	2.84	2.89
$\text{Co}_{0.1}\text{Fe}_{0.9}\text{Al}_2\text{O}_4$	$1300^\circ\text{C}$	0	64.4	35.6	1.81	-
	$1300^\circ\text{C}$	6.4	73.3	20.3	3.92	4.55

<sup>1</sup>The ratio  $\text{Fe}^x/\text{Fe}^{3+}$  is adjusted taking in consideration the number of transferred electrons with  $(\text{peak area of Fe}^0 \times 3 + \text{peak area of Fe}^{2+})/\text{peak area of Fe}^{3+}$ .

#### 4. Conclusions

In this work, solid-state kinetic analysis was performed on four spinel aluminate samples ( $\text{FeAl}_2\text{O}_4$  (0% Co),  $\text{Co}_{0.05}\text{Fe}_{0.95}\text{Al}_2\text{O}_4$  (5% Co),  $\text{Co}_{0.25}\text{Fe}_{0.75}\text{Al}_2\text{O}_4$  (25% Co), and  $\text{Co}_{0.40}\text{Fe}_{0.60}\text{Al}_2\text{O}_4$  (40% Co)) to model their oxidation kinetics in  $\text{CO}_2$  splitting experiments. Thermogravimetric analysis was utilized to measure the conversion over time at four oxidation temperatures ranging from  $1200^\circ\text{C}$  to  $1350^\circ\text{C}$ . Measured gas production ranged from  $158 \mu\text{mol CO/g}$  for the 40% Co sample at  $1350^\circ\text{C}$  to  $997 \mu\text{mol CO/g}$  for the 0% Co sample at  $1200^\circ\text{C}$ . Utilizing a conventional isothermal model-fitting method, the F1 model representing first-order kinetics was found to most accurately represent the experimental data over the conversion range of  $\alpha = 0.20 - 0.70$  for all of the materials studied. The computed rate constants, activation energies, and pre-exponential factors all increase with increasing cobalt content based on this F1 model. The rate constant increased by up to a factor of 4 with the incorporation of cobalt into the sample. In-situ XPS analysis indicates that the rate is enhanced in the cobalt-containing samples due the presence of metallic Co and Fe species on the surface of the reduced cobalt-iron aluminate surface. These metallic species provide alternative sites for the  $\text{CO}_2$  splitting reaction which are not present on

the surface of hercynite and only require one neighboring transition metal site. The presence of these sites in the cobalt-aluminate compounds is found to enhance the rate of reaction through an increased pre-exponential factor.

## **5. Acknowledgments**

This research was supported by the U.S. Department of Energy's Office of Energy Efficiency and Renewable Energy, Fuel Cells Technologies Office Award No. DE-EE0008088, "Computationally Accelerated Discovery and Experimental Demonstration of High-Performance Materials for Advanced Solar Thermochemical Hydrogen Production" and U.S. Department of Energy's Office of Energy Efficiency and Renewable Energy, Fuel Cells Technologies Office Award No. DE-EE006671 "Flowing Particle Bed Solarthermal Redox Process to Split Water."

## **6. References**

- [1] Z. Wang, R.R. Roberts, G.F. Naterer, K.S. Gabriel, Comparison of thermochemical, electrolytic, photoelectrolytic and photochemical solar-to-hydrogen production technologies, *International Journal of Hydrogen Energy*, 37 (2012) 16287-16301.
- [2] C.L. Muhich, B.D. Ehrhart, I. Al-Shankiti, B.J. Ward, C.B. Musgrave, A.W. Weimer, A review and perspective of efficient hydrogen generation via solar thermal water splitting, *Wiley Interdisciplinary Reviews: Energy and Environment*, 5 (2015) 261-287.
- [3] A. Steinfeld, Solar thermochemical production of hydrogen—a review, *Solar Energy*, 78 (2005) 603-615.
- [4] C. Perkins, A.W. Weimer, Solar-thermal production of renewable hydrogen, *AIChE Journal*, 55 (2009) 286-293.
- [5] T. Nakamura, Hydrogen production from water utilizing solar heat at high temperatures, *Solar Energy*, 19 (1977) 467-475.

- [6] J.R. Scheffe, A. Steinfeld, Oxygen exchange materials for solar thermochemical splitting of H<sub>2</sub>O and CO<sub>2</sub>: a review, *Materials Today*, 17 (2014) 341-348.
- [7] S. Abanades, H.I. Villafán-Vidales, CO<sub>2</sub> and H<sub>2</sub>O Conversion to Solar Fuels Via Two-Step Solar Thermochemical Looping Using Iron Oxide Redox Pairs, *Chem. Eng. J.*, 175 (2011) 368.
- [8] W.C. Chueh, C. Falter, M. Abbott, D. Scipio, P. Furler, S.M. Haile, A. Steinfeld, High-Flux Solar-Driven Thermochemical Dissociation of CO<sub>2</sub> and H<sub>2</sub>O using Nonstoichiometric Ceria, *Science*, 330 (2010) 1797-1801.
- [9] Y. Lu, L. Zhu, C. Agrafiotis, J. Vieten, M. Roeb, C. Sattler, Solar fuels production: Two-step thermochemical cycles with cerium-based oxides, *Progress in Energy and Combustion Science*, 75 (2019) 100785.
- [10] I. Al-Shankiti, B.D. Ehrhart, A.W. Weimer, Isothermal redox for H<sub>2</sub>O and CO<sub>2</sub> splitting – A review and perspective, *Solar Energy*, 156 (2017) 21-29.
- [11] R. Bader, L.J. Venstrom, J.H. Davidson, W. Lipiński, Thermodynamic Analysis of Isothermal Redox Cycling of Ceria for Solar Fuel Production, *Energy & Fuels*, 27 (2013) 5533-5544.
- [12] Y. Hao, C.K. Yang, S.M. Haile, High-temperature isothermal chemical cycling for solar-driven fuel production, *Phys Chem Chem Phys*, 15 (2013) 17084-17092.
- [13] L.J. Venstrom, R.M. De Smith, Y. Hao, S.M. Haile, J.H. Davidson, Efficient Splitting of CO<sub>2</sub> in an Isothermal Redox Cycle Based on Ceria, *Energy & Fuels*, 28 (2014) 2732-2742.
- [14] R. Michalsky, V. Botu, C.M. Hargus, A.A. Peterson, A. Steinfeld, Design Principles for Metal Oxide Redox Materials for Solar-Driven Isothermal Fuel Production, *Adv. Energy Mater.*, 5 (2015).

- [15] C.L. Muhich, B.W. Evanko, K.C. Weston, P. Lichty, X. Liang, J. Martinek, C.B. Musgrave, A.W. Weimer, Efficient Generation of H<sub>2</sub> by Splitting Water with an Isothermal Redox Cycle, *Science*, 341 (2013) 540-542.
- [16] A. Steinfeld, Solar hydrogen production via a two-step water-splitting thermochemical cycle based on Zn/ZnO redox reactions, *International Journal of Hydrogen Energy*, 27 (2002) 611-619.
- [17] P.G. Loutzenhiser, A. Meier, A. Steinfeld, Review of the two-step H<sub>2</sub>O/CO<sub>2</sub>-splitting solar thermochemical cycle based on Zn/ZnO redox reactions, *Materials*, 3 (2010) 4922-4938.
- [18] G. Levêque, S. Abanades, J.-C. Jumas, J. Olivier-Fourcade, Characterization of Two-Step Tin-Based Redox System for Thermochemical Fuel Production from Solar-Driven CO<sub>2</sub> and H<sub>2</sub>O Splitting Cycle, *Industrial & Engineering Chemistry Research*, 53 (2014) 5668-5677.
- [19] I. Vishnevetsky, M. Epstein, Tin as a Possible Candidate for Solar Thermochemical Redox Process for Hydrogen Production, *Journal of Solar Energy Engineering*, 131 (2009) 021007-021008.
- [20] A. Steinfeld, S. Sanders, R. Palumbo, Design Aspects of Solar Thermochemical Engineering - A Case Study: Two-Step Water-Splitting Cycle Using the Fe<sub>3</sub>O<sub>4</sub>/FeO Redox System, *Solar Energy*, 65 (1999) 43-53.
- [21] M. Roeb, M. Neises, N. Monnerie, F. Call, H. Simon, C. Sattler, M. Schmücker, R. Pitz-Paal, Materials-Related Aspects of Thermochemical Water and Carbon Dioxide Splitting: A Review, *Materials*, 5 (2012) 2015-2054.
- [22] M. Chambon, S. Abanades, G. Flamant, Solar thermal reduction of ZnO and SnO<sub>2</sub>: Characterization of the recombination reaction with O<sub>2</sub>, *Chemical Engineering Science*, 65 (2010) 3671-3680.

- [23] P. Lichty, X. Liang, C. Muhich, B. Evanko, C. Bingham, A.W. Weimer, Atomic layer deposited thin film metal oxides for fuel production in a solar cavity reactor, *International Journal of Hydrogen Energy*, 37 (2012) 16888-16894.
- [24] T. Kodama, Y. Nakamuro, T. Mizuno, A Two-Step Thermochemical Water Splitting by Iron-Oxide on Stabilized Zirconia, *Journal of Solar Energy Engineering*, 128 (2004) 3-7.
- [25] R.J. Carrillo, J.R. Scheffe, Advances and trends in redox materials for solar thermochemical fuel production, *Solar Energy*, 156 (2017) 3-20.
- [26] D.R. Barcellos, M.D. Sanders, J. Tong, A.H. McDaniel, R.P. O'Hayre,  $\text{BaCe}_{0.25}\text{Mn}_{0.75}\text{O}_{3-\delta}$  - a promising perovskite-type oxide for solar thermochemical hydrogen production, *Energy Environ. Sci.*, 11 (2018) 3256-3265.
- [27] J.R. Scheffe, J. Li, A.W. Weimer, A spinel ferrite/hercynite water-splitting redox cycle, *International Journal of Hydrogen Energy*, 35 (2010) 3333-3340.
- [28] C.L. Muhich, B.D. Ehrhart, V.A. Witte, S.L. Miller, E.N. Coker, C.B. Musgrave, A.W. Weimer, Predicting the solar thermochemical water splitting ability and reaction mechanism of metal oxides: a case study of the hercynite family of water splitting cycles, *Energy Environ. Sci.*, 8 (2015) 3687-3699.
- [29] P.M. Pechini, Method of preparing lead and alkaline earth titanates and niobates and coating method using the same to form a capacitor, in, Google Patents, US, 1967.
- [30] B. Bulfin, F. Call, M. Lange, O. Lübben, C. Sattler, R. Pitz-Paal, I.V. Shvets, Thermodynamics of  $\text{CeO}_2$  Thermochemical Fuel Production, *Energy & Fuels*, 29 (2015) 1001-1009.
- [31] S. Vyazovkin, C.A. Wight, Kinetics in Solids, *Annual Review of Physical Chemistry*, 48 (1997) 125-149.

- [32] L. Fedunik-Hofman, A. Bayon, S.W. Donne, Kinetics of Solid-Gas Reactions and Their Application to Carbonate Looping Systems, *Energies*, 12 (2019) 2981.
- [33] A. Khawam, D.R. Flanagan, Basics and Applications of Solid-State Kinetics: A Pharmaceutical Perspective, *Journal of Pharmaceutical Sciences*, 95 (2006) 472-498.
- [34] C.L. Muhich, K.C. Weston, D. Arifin, A.H. McDaniel, C.B. Musgrave, A.W. Weimer, Extracting Kinetic Information from Complex Gas–Solid Reaction Data, *Industrial & Engineering Chemistry Research*, 54 (2014) 4113-4122.
- [35] J.R. Scheffe, A.H. McDaniel, M.D. Allendorf, A.W. Weimer, Kinetics and mechanism of solar-thermochemical H<sub>2</sub> production by oxidation of a cobalt ferrite–zirconia composite, *Energy Environ. Sci.*, 6 (2013) 963.
- [36] D. Arifin, A.W. Weimer, Kinetics and mechanism of solar-thermochemical H<sub>2</sub> and CO production by oxidation of reduced CeO<sub>2</sub>, *Solar Energy*, 160 (2018) 178-185.
- [37] Q. Jiang, J. Tong, G. Zhou, Z. Jiang, Z. Li, C. Li, Thermochemical CO<sub>2</sub> splitting reaction with supported La<sub>x</sub>A<sub>1-x</sub>Fe<sub>y</sub>B<sub>1-y</sub>O<sub>3</sub> (A=Sr, Ce, B=Co, Mn; 0 ≤ x, y ≤ 1) perovskite oxides, *Solar Energy*, 103 (2014) 425-437.
- [38] R.C. Baetzold, G.A. Somorjai, Preexponential factors in surface reactions, *Journal of Catalysis*, 45 (1976) 94-105.
- [39] C.T. Campbell, J.R.V. Sellers, Enthalpies and Entropies of Adsorption on Well-Defined Oxide Surfaces: Experimental Measurements, *Chem Rev*, 113 (2013) 4106-4135.
- [40] C.T. Campbell, L. Árnadóttir, J.R.V. Sellers, Kinetic Prefactors of Reactions on Solid Surfaces, in: *Zeitschrift für Physikalische Chemie*, 2013, pp. 1435.

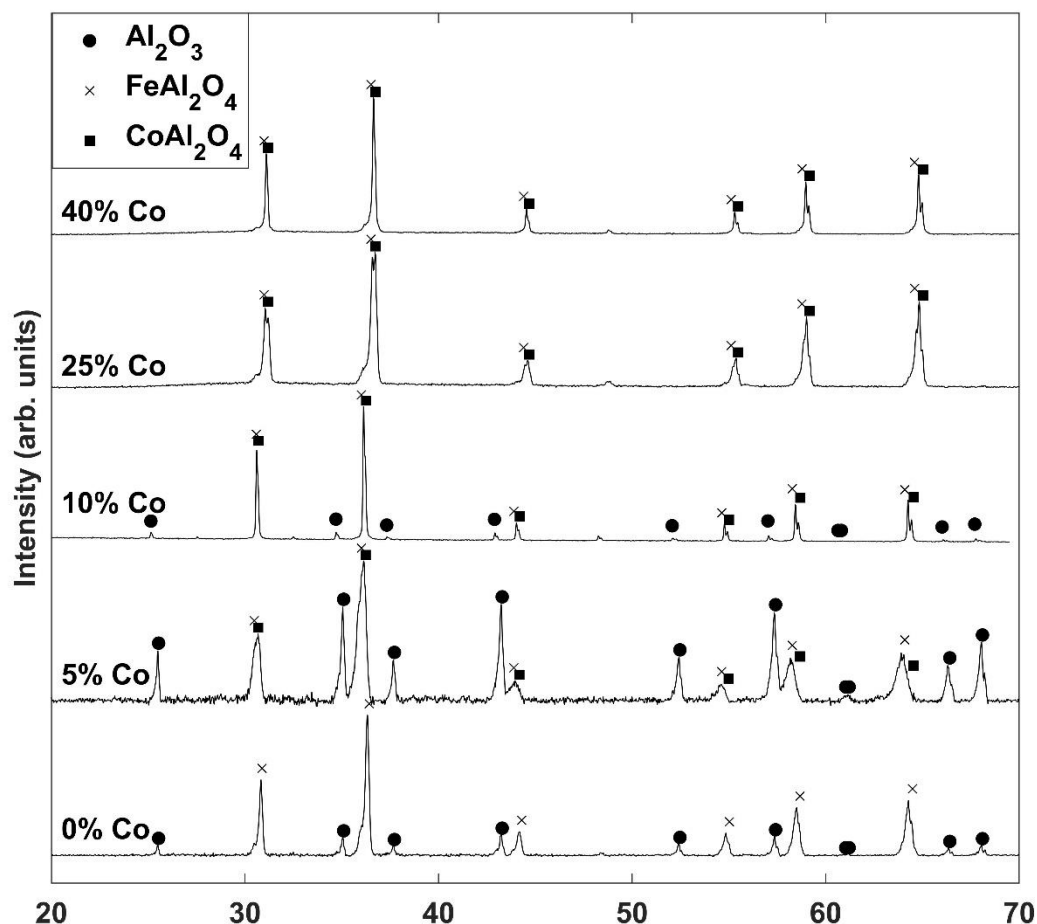
- [41] R.S. Smith, Z. Li, L. Chen, Z. Dohnálek, B.D. Kay, Adsorption, Desorption, and Displacement Kinetics of H<sub>2</sub>O and CO<sub>2</sub> on TiO<sub>2</sub>(110), *The Journal of Physical Chemistry B*, 118 (2014) 8054-8061.
- [42] S. Piccinin, M. Stamatakis, CO Oxidation on Pd(111): A First-Principles-Based Kinetic Monte Carlo Study, *ACS Catalysis*, 4 (2014) 2143-2152.
- [43] J. Hulva, Z. Jakub, Z. Novotny, N. Johansson, J. Knudsen, J. Schnadt, M. Schmid, U. Diebold, G.S. Parkinson, Adsorption of CO on the Fe<sub>3</sub>O<sub>4</sub>(001) Surface, *The Journal of Physical Chemistry B*, 122 (2018) 721-729.
- [44] T. Lin, K. Gong, C. Wang, Y. An, X. Wang, X. Qi, S. Li, Y. Lu, L. Zhong, Y. Sun, Fischer–Tropsch Synthesis to Olefins: Catalytic Performance and Structure Evolution of Co<sub>2</sub>C-Based Catalysts under a CO<sub>2</sub> Environment, *ACS Catalysis*, 9 (2019) 9554-9567.
- [45] Q. Lin, B. Liu, F. Jiang, X. Fang, Y. Xu, X. Liu, Assessing the formation of cobalt carbide and its catalytic performance under realistic reaction conditions and tuning product selectivity in a cobalt-based FTS reaction, *Catalysis Science & Technology*, 9 (2019) 3238-3258.
- [46] B. Zhang, X. Wu, R. Zhou, Calculation of oxygen self-diffusion coefficients in Mg<sub>2</sub>SiO<sub>4</sub> polymorphs and MgSiO<sub>3</sub> perovskite based on the compensation law, *Solid State Ionics*, 186 (2011) 20-28.
- [47] G. Pecchi, M.G. Jiliberto, E.J. Delgado, Reaction Kinetics of Methane Combustion over La<sub>1-x</sub>Ca<sub>x</sub>FeO<sub>3</sub> Perovskites, *Journal of the Chilean Chemical Society*, 56 (2011) 895-900.
- [48] N. Katada, S. Sota, N. Morishita, K. Okumura, M. Niwa, Relationship between activation energy and pre-exponential factor normalized by the number of Brønsted acid sites in cracking of short chain alkanes on zeolites, *Catalysis Science & Technology*, 5 (2015) 1864-1869.

- [49] W.C. Conner, A general explanation for the compensation effect: The relationship between  $\Delta S^\ddagger$  and activation energy, *Journal of Catalysis*, 78 (1982) 238-246.
- [50] S.M. Bashir, H. Idriss, The reaction of propylene to propylene-oxide on CeO<sub>2</sub>: An FTIR spectroscopy and temperature programmed desorption study, *The Journal of Chemical Physics*, 152 (2020) 044712.
- [51] I. Jastrzębska, J. Szczerba, P. Stoch, A. Błachowski, K. Ruebenbauer, R. Prorok, E. Śnieżek, Crystal structure and Mössbauer study of FeAl<sub>2</sub>O<sub>4</sub>, 60 (2015) 47.
- [52] M. Xue, Q. Guo, Study on growth mechanisms and electronic structures of polar NiO(111) ultrathin films using iron oxide buffer layers, *Journal of Alloys and Compounds*, 598 (2014) 224-229.
- [53] S.D. Senanayake, G.I.N. Waterhouse, A.S.Y. Chan, T.E. Madey, D.R. Mullins, H. Idriss, Probing Surface Oxidation of Reduced Uranium Dioxide Thin Film Using Synchrotron Radiation, *The Journal of Physical Chemistry C*, 111 (2007) 7963-7970.
- [54] H. Idriss, C. Diagne, J.P. Hindermann, A. Kiennemann, M.A. Barteau, Reactions of Acetaldehyde on CeO<sub>2</sub> and CeO<sub>2</sub>-Supported Catalysts, *Journal of Catalysis*, 155 (1995) 219-237.
- [55] J. Bennet, R. Tholkappiyar, K. Vishista, N.V. Jaya, F. Hamed, Attestation in self-propagating combustion approach of spinel AFe<sub>2</sub>O<sub>4</sub> (A=Co, Mg and Mn) complexes bearing mixed oxidation states: Magnetostructural properties, *Applied Surface Science*, 383 (2016) 113-125.
- [56] P. Singh, K.M.K. Srivatsa, A. Barvat, P. Pal, X-ray photoelectron spectroscopic studies of CeO<sub>2</sub> thin films deposited on Ni-W (100), c-Al<sub>2</sub>O<sub>3</sub> (0001) and Si (100) substrates, *Current Applied Physics*, 16 (2016) 1388-1394.

[57] G.H. Rocker, Experimental studies of the defect structure of the  $\text{TiO}_2(110)$  surface before and after the exposure to oxygen, hydrogen and carbon monoxide, in: Department of Physics, Montana State University, Bozeman, 1985, pp. 269.

[58] M.A. Henderson, C.L. Perkins, M.H. Engelhard, S. Thevuthasan, C.H.F. Peden, Redox properties of water on the oxidized and reduced surfaces of  $\text{CeO}_2(111)$ , *Surface Science*, 526 (2003) 1-18.

## 7. Supplemental Information



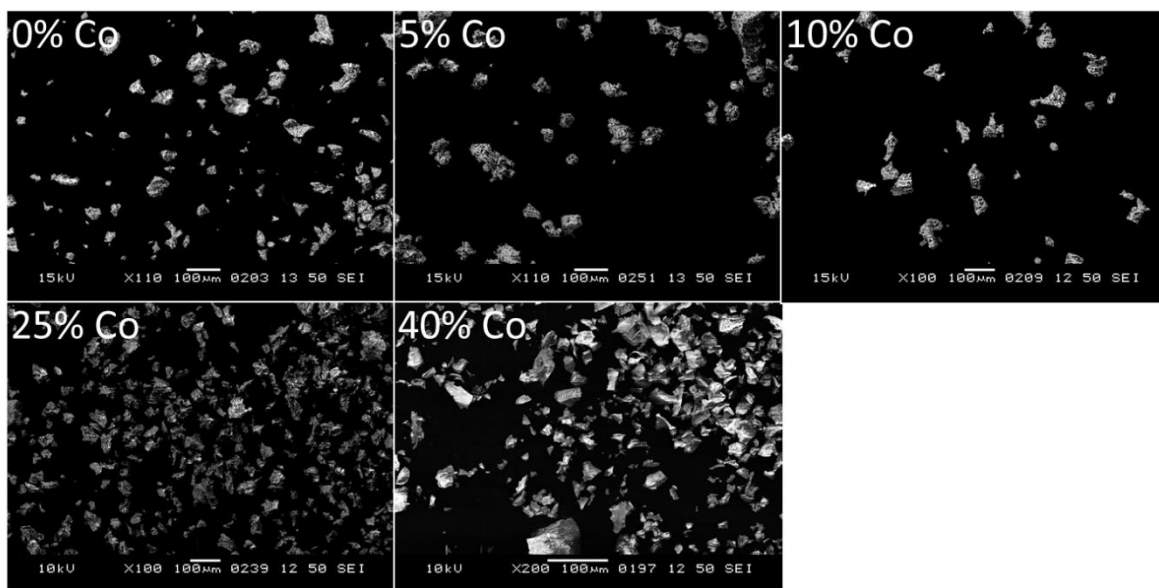


Figure S2. SEM images before cycling for the five compositions used in the TGA and XPS experiments: 0% Co, 5% Co, 10% Co, 25% Co, and 40% Co.

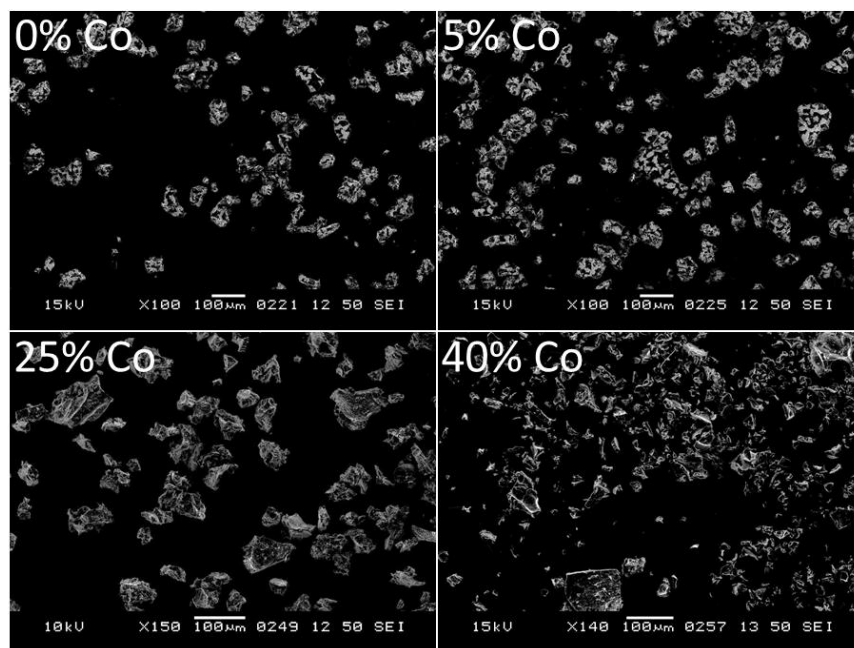


Figure S3. SEM images after cycling for the four compositions used in the TGA experiments: 0% Co, 5% Co, 25% Co, and 40% Co. Due to the small sample size utilized in XPS, SEM of the 10% sample could not be obtained.

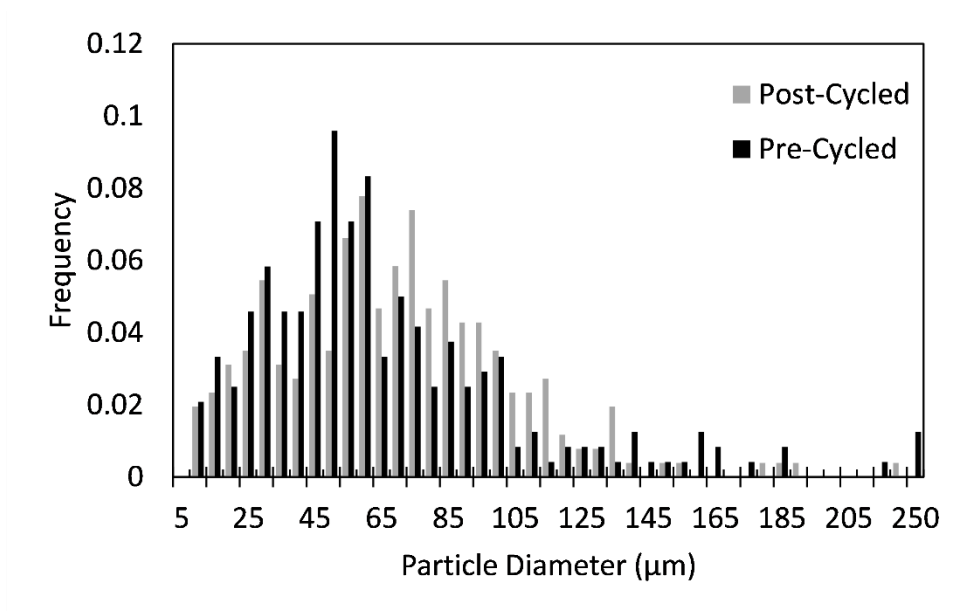


Figure S4. Particle size distributions before (black) and after (grey) cycling for the 0% Co sample. The average particle diameters before and after cycling were  $67 \pm 34 \mu\text{m}$  and  $64 \pm 41 \mu\text{m}$ , respectively, which was determined to not be statistically significantly different.

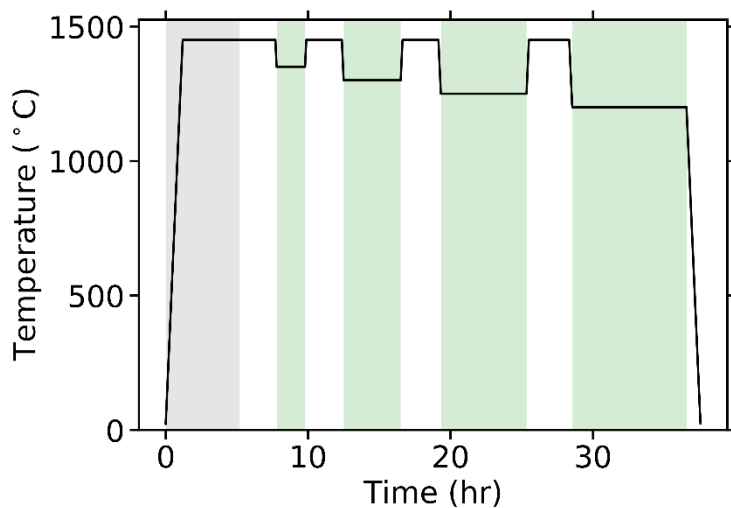


Figure S5. Example temperature program utilized for the kinetic analysis. Each oxidation step is highlighted in green. The actual times utilized for each oxidation step varied from 2 to 8 hours depending on the temperature and the amount of time required for each material to reach equilibrium. The reduction time and temperature were constant at 150 minutes and  $1450^{\circ}\text{C}$ . The initial ramp and hold at  $1450^{\circ}\text{C}$  to remove existing organics species is highlighted in grey.

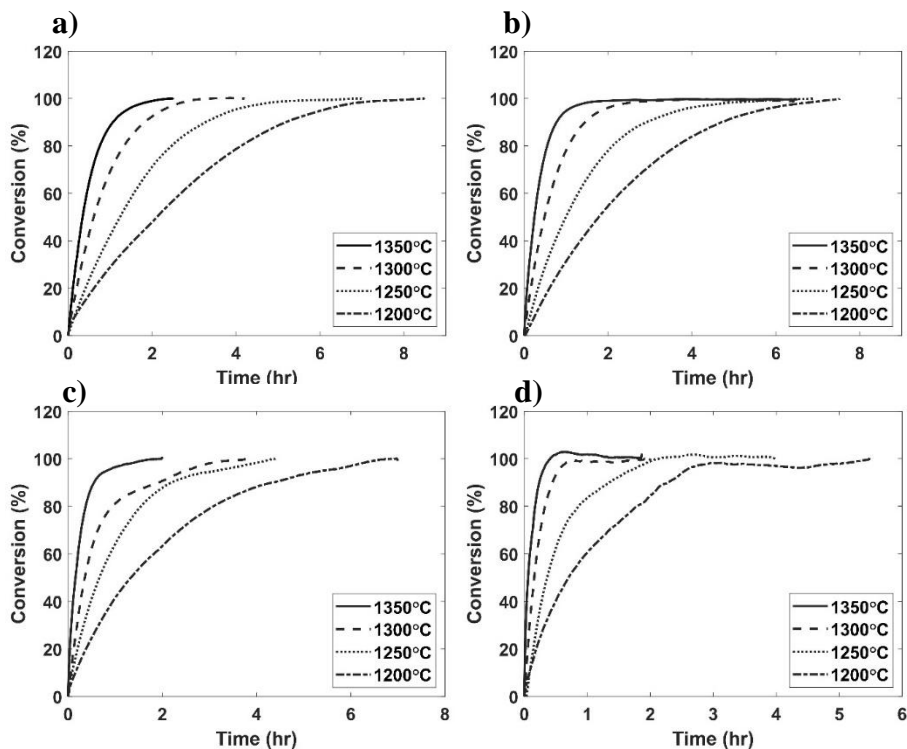


Figure S6. Conversion versus time data extracted from TG mass gain for oxidation in CO<sub>2</sub> at four temperatures of a) FeAl<sub>2</sub>O<sub>4</sub> (0% Co) b) Co<sub>0.05</sub>Fe<sub>0.95</sub>Al<sub>2</sub>O<sub>4</sub> (5% Co) c) Co<sub>0.25</sub>Fe<sub>0.75</sub>Al<sub>2</sub>O<sub>4</sub> (25% Co) and d) Co<sub>0.40</sub>Fe<sub>0.60</sub>Al<sub>2</sub>O<sub>4</sub> (40% Co). All reductions were conducted at 1450°C in Ar.

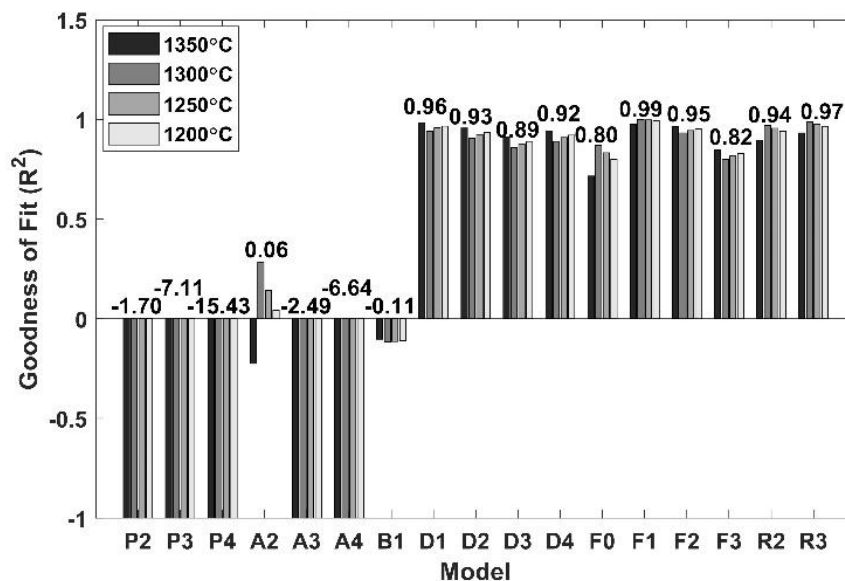


Figure S7. Coefficient of determination for each of the 17 solid-state kinetic models evaluated for the case of 0% Co (FeAl<sub>2</sub>O<sub>4</sub>). The F1 (first-order reaction) model had the best fit with a coefficient of determination > 0.98 for all materials studied.

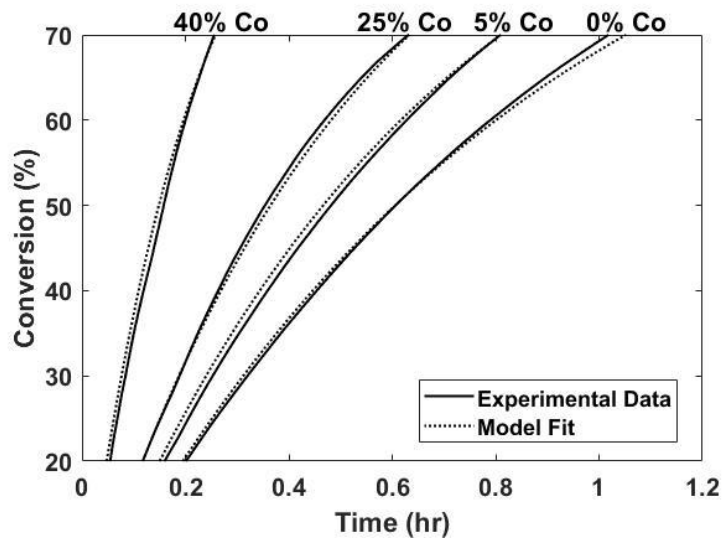


Figure S8. Comparison of the conversion versus time data from experiment and the model fit for each of the materials studied at 1300°C for  $\alpha = 0.20 - 0.70$ .

For both as-prepared samples, the C 1s region shows the presence of large amounts of adventitious graphitic carbon, as is usually the case for powder materials, and the presence of carboxylate (-COO-) species, with a binding energy at ca. 289 eV, left over from the synthesis method. After heating under vacuum, the XPS C 1s contribution decreased considerably in both samples due to the removal of graphitic layers as CO/CO<sub>2</sub>. In the Al 2p region of both compounds, Al<sup>3+</sup> is seen with a peak centered at 74.5 eV corresponding to Al 2p<sub>3/2,1/2</sub> with no change after heating, indicating that Al is not a redox active species, as expected. The O 1s region of the as-prepared oxides is typical for an un-reduced material with the lattice oxygen peak centered at 530.5 eV, a signal for irreversibly adsorbed water at 532.5 eV, and surface hydroxyls at ca. 531.5 eV, which is not deconvoluted in the figure for the sake of simplicity. Upon heating to 1300°C the O 1s region shows a decrease in adsorbed water and a slight shift in the binding energy of the lattice oxygen to 530.8 eV (from 530.5 eV). This shift may be due to some bulk reduction of the oxide material. While no references for the XPS O 1s of reduced FeAl<sub>2</sub>O<sub>4</sub> were found, similar shifts for reduced TiO<sub>2</sub> and reduced CeO<sub>2</sub> are routinely observed [56-58].

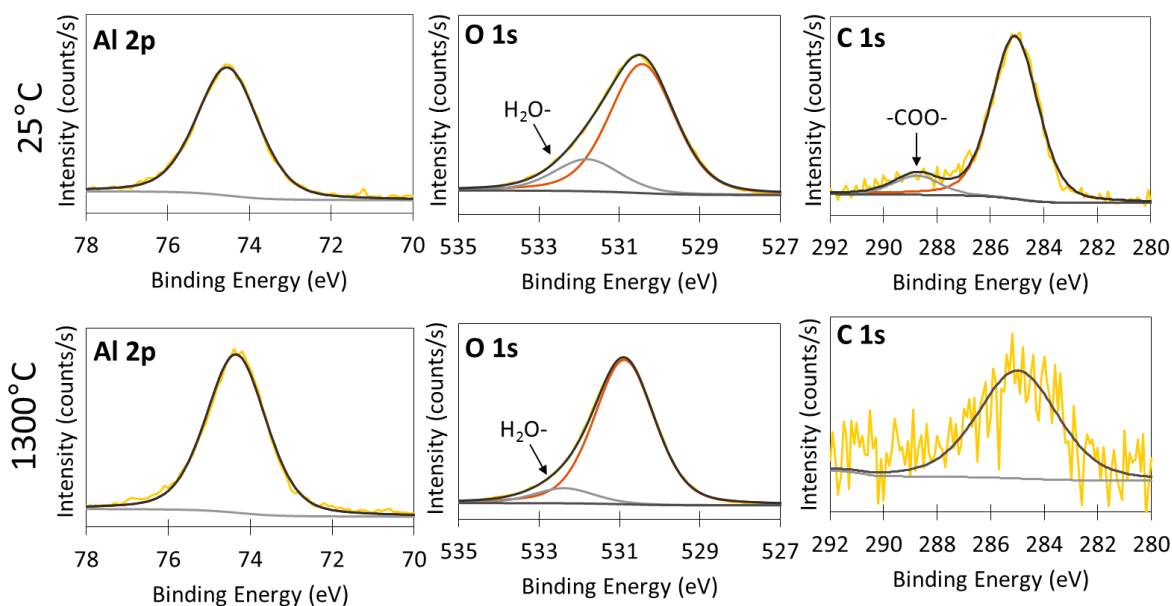


Figure S9. XPS regions for Al 2p, O 1s, and C 1s in FeAl<sub>2</sub>O<sub>4</sub> as-prepared at 25°C (top) and after reducing at 1300°C in vacuum for 5 minutes (bottom).

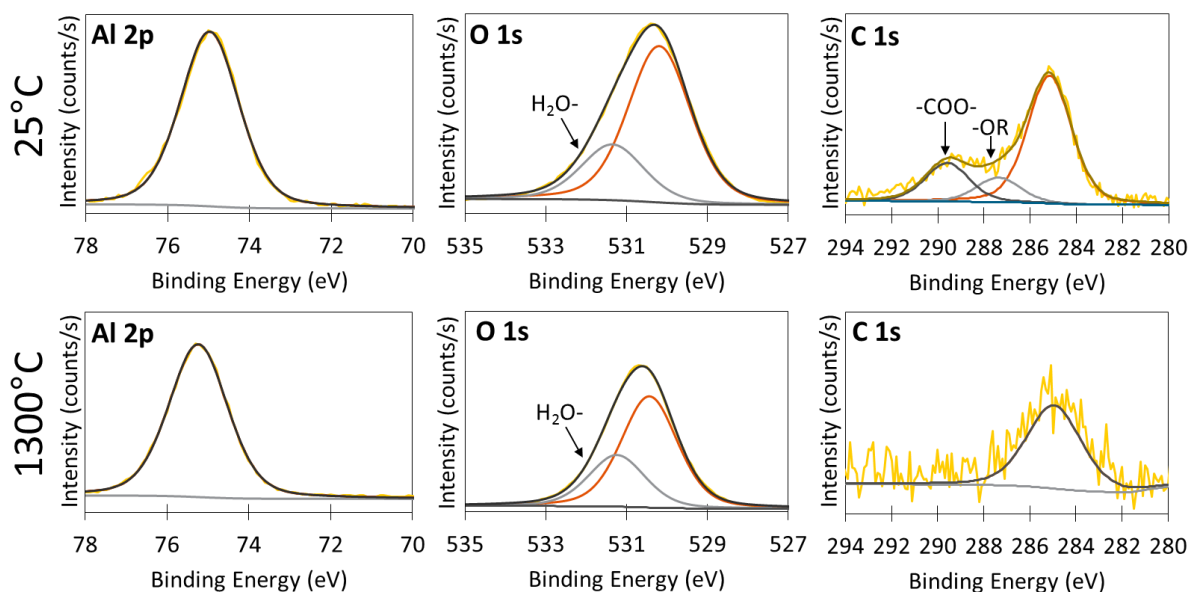


Figure S10. XPS regions for Al 2p, O 1s, and C 1s in Co<sub>0.1</sub>Fe<sub>0.9</sub>Al<sub>2</sub>O<sub>4</sub> as prepared at 25°C (top) and after reducing at 1300°C in vacuum for 5 minutes (bottom).